

Retraction

Retracted: Deep Learning-Based Crack Monitoring for Ultra-High Performance Concrete (UHPC)

Journal of Advanced Transportation

Received 8 August 2023; Accepted 8 August 2023; Published 9 August 2023

Copyright © 2023 Journal of Advanced Transportation. This is an open access article distributed under the Creative Commons Attribution License, which permits unrestricted use, distribution, and reproduction in any medium, provided the original work is properly cited.

This article has been retracted by Hindawi following an investigation undertaken by the publisher [1]. This investigation has uncovered evidence of one or more of the following indicators of systematic manipulation of the publication process:

- (1) Discrepancies in scope
- (2) Discrepancies in the description of the research reported
- (3) Discrepancies between the availability of data and the research described
- (4) Inappropriate citations
- (5) Incoherent, meaningless and/or irrelevant content included in the article
- (6) Peer-review manipulation

The presence of these indicators undermines our confidence in the integrity of the article's content and we cannot, therefore, vouch for its reliability. Please note that this notice is intended solely to alert readers that the content of this article is unreliable. We have not investigated whether authors were aware of or involved in the systematic manipulation of the publication process.

Wiley and Hindawi regrets that the usual quality checks did not identify these issues before publication and have since put additional measures in place to safeguard research integrity.

We wish to credit our own Research Integrity and Research Publishing teams and anonymous and named external researchers and research integrity experts for contributing to this investigation.

The corresponding author, as the representative of all authors, has been given the opportunity to register their agreement or disagreement to this retraction. We have kept a record of any response received.

References

- [1] D. Wu, H. Zhang, and Y. Yang, "Deep Learning-Based Crack Monitoring for Ultra-High Performance Concrete (UHPC)," *Journal of Advanced Transportation*, vol. 2022, Article ID 4117957, 10 pages, 2022.

Research Article

Deep Learning-Based Crack Monitoring for Ultra-High Performance Concrete (UHPC)

Dongling Wu,¹ Hongxiang Zhang ,¹ and Yiying Yang²

¹School of Civil Engineering, Northeast Forestry University, Harbin 150040, China

²School of Business Administration, Harbin Cambridge University, Harbin 150069, China

Correspondence should be addressed to Hongxiang Zhang; ldzhldzhx@163.com

Received 9 March 2022; Revised 12 April 2022; Accepted 30 April 2022; Published 15 June 2022

Academic Editor: Lingwei Xu

Copyright © 2022 Dongling Wu et al. This is an open access article distributed under the Creative Commons Attribution License, which permits unrestricted use, distribution, and reproduction in any medium, provided the original work is properly cited.

In civil engineering, image recognition technology in artificial intelligence is widely used in structural damage detection. Traditional crack monitoring based on concrete images uses image processing, which requires high image preprocessing techniques, and the results of detection are vulnerable to factors, such as lighting and noise. In this study, the full convolutional neural networks FCN-8s, FCN-16s, and FCN-32s are applied to monitoring of concrete apparent cracks and according to the image characteristics of concrete cracks and experimental results. The FCN-8s model was tested with a correct crack monitoring rate of 0.6721, while the new network model had a correct crack detection rate of 0.7585, a significant improvement in the correct crack detection rate.

1. Introduction

Concrete is an important infrastructure for the development of the national economy, the development of concrete to strengthen the links between various cities, thus promoting the economic development of all walks of life, and with the economic development of the country, there will be a large number of construction of roads. Although road construction has been developing, but cannot just focus on the constant construction of new roads and not focus on road maintenance, road maintenance and repair and road construction are equally important [1].

With the construction of a large number of roads and the increase in road density, the health of roads requires even more close attention. With the spread of the automobile, many old roads are experiencing increasing traffic volumes that have long exceeded the standards for which they were designed. Because of the road surface in the long-term load and frequent natural disasters, damage, and the emergence of cracks, structural strength continues to decline, affecting the safety of traffic; even if the cracks are left less serious, the presence of too many will not only affect the comfort of driving and affect the aesthetics but also the potential safety risks, so for the location of the road damage, certain

measures should be taken to extend the life of the structure [2, 3] and to prevent road accidents from occurring [4, 5]. However, with the large number of roads and the changing condition of the pavement, it is not realistic to perfectly and strictly control the integrity of each road, and it is important to take appropriate measures to regularly record the health of each road and provide recommendations for its repair based on the actual condition of each road. Therefore, for pavement works, a proper assessment of the health of the road is essential for the rehabilitation of the road.

Assessing the health of a road is not an easy task, as the complexity of the road surface makes it difficult to collect information on the road surface, but with the development of technology, today's camera equipment can now take real-time pictures of the road surface at certain moving speeds, so we can both use the massive amount of photos taken by a car with the ability to take pictures of a section of the road surface and use them as statistical data in the form of big data [6]. However, for a large amount of photo data, it is obviously not appropriate to take manual statistics, so machine learning can be used to train a learner capable of recognizing cracks through a large number of crack samples to recognize and count the large amount of photos, while the learner can also be used for real-time inspection by inspecting vehicles;

the recognition accuracy of the learner is crucial to be able to correctly assess the health of the road. The study of road crack recognition algorithms is of great significance [7].

2. Related Work

With the development of computer technology, researchers at home and abroad have come up with their own crack extraction solutions. With the development of pavement photography technology, CCD cameras are commonly used to capture images of pavement cracks [8]. With traditional digital image crack detection algorithms, the captured crack images can be processed to analyze the location where they are located in the image. Wang et al. [9] combined feature extraction of cracks by Sobel's operator combined with the iterative threshold segmentation method and morphology [10]. Yang et al. [11] proposed an improved Sobel operator to do feature extraction of pavement cracks with remarkable results. In addition, many researchers have used the Sobel operator for crack feature extraction [12]. In [13], an improved Canny operator was proposed for feature extraction of pavement cracks, and it was demonstrated that the improved Canny operator was more effective in denoising cracks than the improved one before [14]. In [15], an application was designed to detect the width of cracks by processing images with the Canny operator in conjunction with Android development [16]. In addition to this, many researchers have used the Canny operator for crack feature extraction [17].

Crack detection based on SVM is usually performed by manually tagging the cracked and noncracked images after image processing with classification labels and training the trained model for crack recognition by the SVM algorithm. Wang Yixin segmented the image by an improved DBC algorithm, extracted cracks by a threshold detection algorithm, and then recognized the cracks by the traditional SVM algorithm [18]. Wang et al. [19] designed feature images of different scales to identify noise, cracks, and background pavement by training a classifier through SVM. In addition to this, a number of researchers have used SVM algorithms for crack recognition [20].

Similar to SVM, BP neural network-based crack detection also requires a model trained on a large number of images to identify cracks, except that the BP neural network simulates a computational model defined by the human brain. In [21], unprocessed native images were used to train a BP neural network, which did not work well. Garcia et al. [10] proposed an improved median filter algorithm combined with an area contrast algorithm for crack feature extraction, classification, and recognition using a BP neural network. In [11], cracks were extracted by median filtering and noise reduction through Sobel's operator, and finally, a BP neural network was constructed to identify these cracks. In addition, many researchers have used BP neural networks for crack recognition [12].

The deep learning-based convolutional neural network is also a type of the neural network, which is able to learn deeper features in images compared to shallow neural networks. Kou Xiao used a grey-scale feature algorithm to extract crack features and used a convolutional neural network for crack training recognition via the deep learning

framework Caffe [13]. In [14], the image was binarized by threshold segmentation of the crack image, and then, the binarized image was flagged with a connected domain, and the rectangular parameters of the connected domain were denoised to extract features, which were then trained for recognition by the convolutional neural network AlexNet [15]. Due to the rapid development of computer technology in recent years, convolutional neural networks have been used in large numbers for image recognition in recent years, so there are also many researchers using convolutional neural networks for crack recognition [16].

3. Dataset Creation

One hundred and twenty-five (3120×4160) images of cracked concrete were taken as the original dataset, of which 35 images were taken as the test set and the remaining 90 images were used for training and validation of the convolutional neural network. The network used in this study has a fixed size requirement for input images, so the samples need to be sliced and deflated, and this process is carried out through a MATLAB program.

Before the network is trained, all training samples need to be labelled, i.e., the class of each training sample needs to be determined. One method of labelling is to first slice the original image collection into smaller samples and then label each sample. This method has many drawbacks, such as the number of samples needed for network training is huge, and manually classifying the samples one by one is undoubtedly a tedious and time-consuming task; for some images with obscure image features, different people may have different classification results for the same sample, and the manual classification method is highly subjective. As crack images are cut into small samples, people lose other reference information in the original images for sample labelling, and it causes people to classify the samples inaccurately. Therefore, this study applies a semiautomatic labelling method [17] to circumvent these drawbacks.

Cracked samples can be broadly classified into three categories according to the learning difficulty of the network: the first category of cracks are in the central region of the sample, such samples have obvious features and are easy for the network to learn, as shown in Figure 1(a); the second category of cracks are at the edges of the sample, but have sufficient length to make it easier for the network to learn their features, as shown in Figure 1(b); the third category is when cracks exist at the edges of the sample and have a short length, it is difficult for the network to learn and detect such samples, as shown in Figure 1(b). These samples are referred to as fuzzy samples, as shown in Figures 1(c) and 1(d). In traditional crack detection methods, fuzzy samples are often discarded from training samples because they are prone to misclassification. In this study, two classification criteria are used to compare the effect of sample discard on crack detection.

4. Full Convolutional Neural Network Crack Detection

4.1. Improved FCN-8s Crack Detection Model Based on Cavity Convolution. FCN-8s performed best in crack detection, but its crack accuracy (CA) was only 67.21%, leaving much room

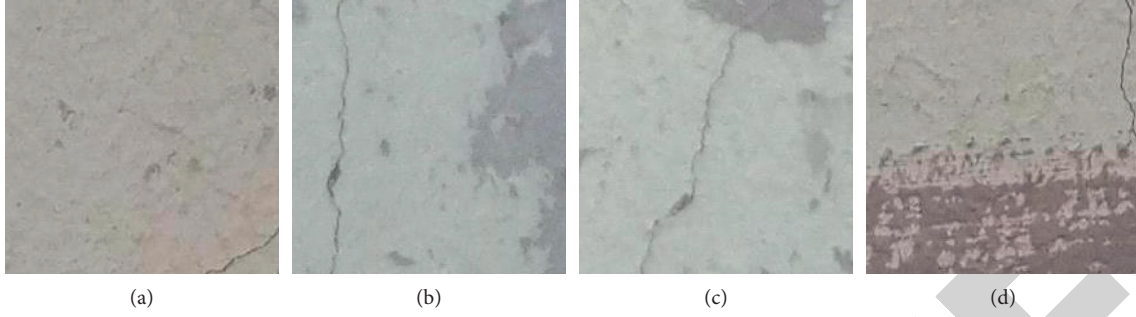


FIGURE 1: Sample cracks. (a) Short cracks at edges. (b) Central cracks. (c) Short cracks at corners. (d) Long cracks at edges.

for improvement. 53.05%, 46.86%, and 67.21% were achieved by FCN-32s, FCN-16s, and FCN-8s, respectively, with FCN-16s being the worst performer. FCN-16s added more front-end feature map information to the network than FCN-32s, i.e., the inclusion of the feature map extracted by convolution module 4 (conv4) did not contribute to crack detection. This is due to the fact that the front-end convolution of the network has a smaller field of perception and some of the features extracted from the concrete surface are partially similar to the feature information of the cracks. This part of information can interfere with the network learning crack features, so the perception of convolution module 4 should be expanded appropriately. In this way, the convolutional module 4 can extract a larger range of information, allowing the network to better learn the difference between the crack and its similar parts.

The cost function of the warp network is

$$J(w, b) = \frac{1}{m} \sum_{i=1}^m J(w, b; x^{(i)}, y^{(i)}), \quad (1)$$

$$J(w, b; x^{(i)}, y^{(i)}) = \frac{1}{2} (y^{(i)} - h_{w,b}(x^{(i)}))^2.$$

The overall cost of the network is the average cost of all training samples.

We are trying to find the best w, b that minimizes the value of $J(w, b)$ and the cost function, so J is a function on w, b , where w, b is also not a scalar, but a set of many w_{ij}, b_{ij} s. The expression for w, b is not explicitly seen in the cost function because it is replaced by the concise $h_{w,b}(x^{(i)})$. Therefore, it is important to emphasize that only w, b is a variable in the expanded expression of J (assuming it can be expanded), and the rest is known. Therefore, according to the idea of gradient descent, for each $w_{ij}^{(l)}, b_{ij}^{(l)}$, we simply update in the direction of the negative gradient, i.e.,

$$w_{ij}^{(l)} := w_{ij}^{(l)} - \alpha \frac{\partial J}{\partial w_{ij}^{(l)}}, \quad (2)$$

$$b_{ij}^{(l)} := b_{ij}^{(l)} - \alpha \frac{\partial J}{\partial b_{ij}^{(l)}}.$$

The vectorized expression is

$$\begin{aligned} w^{(l)} &:= w^{(l)} - \alpha \frac{\partial J}{\partial w^{(l)}}, \\ b^{(l)} &:= b^{(l)} - \alpha \frac{\partial J}{\partial b^{(l)}}, \end{aligned} \quad (3)$$

where α is the learning rate.

Therefore, as long as the partial derivative of w, b can be obtained, it can be updated iteratively, so as to complete the whole algorithm. It seems simple, but it is difficult. Because $J(w, b)$ is difficult to write an explicit expression, it is difficult to find the partial derivative for each w_{ij}, b_{ij} . The main reason is that the network is layered, and then, w, b is layered, which leads to the difficulty of finding the partial derivative and back propagation.

Since w, b is hierarchical, it is natural to find the partial derivatives of w, b in a hierarchical way. Then, it is natural to find a recursive structure to express the bias. Observing the structure $z^{(l+1)} = w^{(l+1)}a^{(l)} + b^{(l+1)}$ in forward conduction, it is natural to find the bias of $w^{(l+1)}, b^{(l+1)}$, by simply asking for the bias of $z^{(l+1)}$ (matrices and vectors are derived in a scalar-like form, $a^{(l)}$ considered as constants).

Considering the case of a single sample, when is the output layer ($l=3$), we have

$$\begin{aligned} \delta^{(3)} &= \frac{\partial J}{\partial z^{(3)}} \\ &= \frac{\partial}{\partial z^{(3)}} \frac{1}{2} (y - h(x))^2 \\ &= \frac{\partial}{\partial z^{(3)}} \frac{1}{2} (y - a^{(3)})^2 \\ &= \frac{\partial}{\partial z^{(3)}} \frac{1}{2} (y - f(z^{(3)}))^2 \\ &= (y - h(x)) \text{of}'(z^{(3)}). \end{aligned} \quad (4)$$

When l is a nonoutput layer (hidden layer) ($l=2$), we have

$$\begin{aligned}
\delta^{(2)} &= \frac{\partial J}{\partial z^{(2)}} \\
&= \frac{\partial J}{\partial z^{(3)}} \cdot \frac{\partial z^{(3)}}{\partial z^{(2)}} \\
&= \delta^{(3)} \cdot \frac{\partial z^{(3)}}{\partial z^{(2)}} \\
&= \delta^{(3)} \cdot \frac{\partial}{\partial z^{(2)}} [w^{(2)} f(z^{(2)}) + b^{(2)}] \\
&= w^{(2)} f'(z^{(2)}) \circ \delta^{(3)}.
\end{aligned} \tag{5}$$

So,

$$\begin{aligned}
\delta^{(L)} &= (y - h(x)) \cdot a^{(L)} \\
\delta^{(l)} &= w^{(l)} a^{(l)} \cdot \delta^{(l+1)}, \quad (l = 2, \dots, L-1) \\
\frac{\partial J}{\partial w^{(l)}} &= \frac{\partial J}{\partial z^{(l)}} \cdot \frac{\partial z^{(l)}}{\partial w^{(l)}} = \delta^{(l)} \cdot (a^{(l-1)})^T \\
\frac{\partial J}{\partial b^{(l)}} &= \frac{\partial J}{\partial z^{(l)}} \cdot \frac{\partial z^{(l)}}{\partial b^{(l)}} = \delta^{(l)}, \quad (l = 2, \dots, L).
\end{aligned} \tag{6}$$

4.2. Null Convolution. The first is to increase the number of convolutions, e.g., 2 layers of 3×3 convolutions can be combined to obtain a 5×5 field of perception, and the second is to use pooling layers, where pooling operation reduces the feature map to make the field of perception of subsequent convolutions relatively larger. The first method increases network parameters less than using 5×5 convolution directly, but the number of convolutions per layer in convolution module 4 is 512, and each additional layer of 3×3 convolution increases the number of parameters by $3 \times 3 \times 512$, which is still a significant increase. The second method does not increase the number of parameters, but loses some of the image information. These cracks themselves have a low number of pixels, and this loss of information may have a detrimental effect on the detection of cracks.

Dilated convolution [18] is a data sampling method that can increase the convolution field while avoiding the problems mentioned above. Figures 2(a) and 2(b) show the size of the convolution field for a convolution kernel size of 3×3 and an expansion factor of 1, 2, and 3, respectively. The field size of null convolution can be calculated from equation (7), where k is the conventional convolution field edge length, r is the expansion factor, and k' is the corresponding null convolution field edge length. Null convolution can make the receptive field grow rapidly with the same number of convolution parameters involved in the calculation, e.g., when three-layer convolution in Figure 2 is coupled, a receptive field of size 13×13 can be obtained, whereas a normal three-layer 3×3 convolution can only obtain a receptive field of size 7×7 .

$$k' = (k - 1)(r - 1) + k. \tag{7}$$

The use of null convolution requires the following rules. (1) The maximum convention of the expansion coefficients of superimposed null convolution cannot be greater than 1. (2) The expansion coefficients of null convolution need to be designed in a sawtooth shape. (3) The expansion coefficients the null convolution need to satisfy equation (8), where M_i is the maximum expansion coefficient of the i^{th} layer and r_i is the expansion coefficient of the i^{th} layer. When the edge length of the convolution kernel is k , we need to let $M_i \leq k$.

$$M_i = \text{Max}[M_{i+1} - 2r_i, M_{i+1} - 2(M_{i+1} - r_i), r_i]. \tag{8}$$

The jagged expansion coefficients help the network to detect information about objects of different sizes in the image, and the other two rules ensure that null convolution utilizes the full pixel value of the image. Figures 3 and 4 show the utilization of this part of the input layer feature map eigenvalues when 3×3 convolution with expansion coefficients of $[2 \ 2 \ 2]$ and $[1 \ 2 \ 9]$ is coupled, respectively. The utilization of the eigenvalues in the layer 2 convolution output, the layer 1 convolution output, and the layer 1 convolution input eigenmap by layer 3 convolution is shown in Figures 3 and 4 in (a), (b), and (c), respectively. These two combinations of null convolution do not conform to rules 1 and 2, respectively, and their convolution operations on the input feature map are discontinuous and do not utilize all the eigenvalues of the input feature map.

4.3. New Network Architecture. From the previous section, it is clear that FCN-8s have the best detection of cracks among the three full convolutional networks, and the extracted feature map of convolutional module 4 is not helpful for crack detection. Therefore, the new network will be based on FCN-8s with modifications to convolutional module 4. Null convolution is used to replace normal convolution in the original convolution module 4, so that the convolution can extract a larger range of information and avoid the network being too sensitive to the detailed information of the image and confusing the cracks with the parts of the concrete background that are similar to it [22].

The size of the feature map output from convolution module 4 is reduced due to the use of null convolution instead of normal convolution in the original convolution module 4. To prevent the feature map size from being too small at the back end of the network, the padding parameter of first convolution in convolution module 1 (conv1) changed from 100 to 150. The detailed parameters of new convolution module 4 are given in Table 1, where the initial input image size is 256×256 pixels when training the network and the feature map size is 69×69 when input to convolution module 4, with a depth of 512. In the following, the improved FCN-8s crack detection model based on null convolution is referred to as the new network.

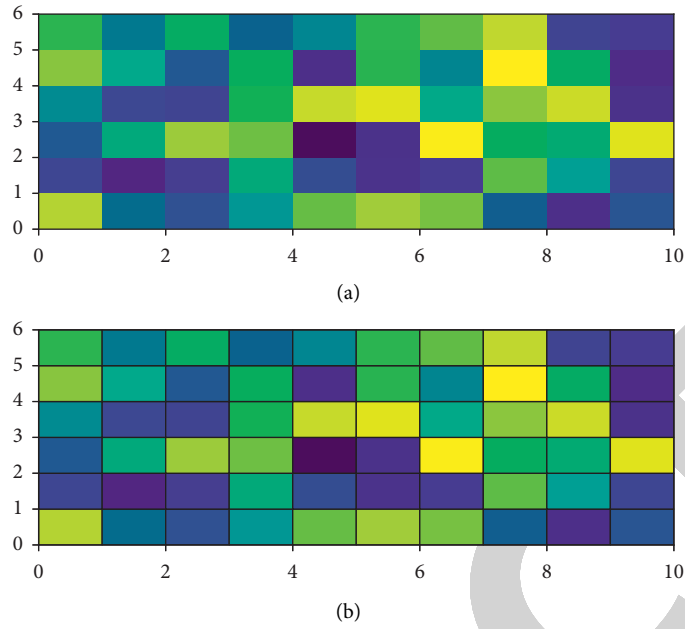


FIGURE 2: Schematic diagram of the convolution field of a cavity. (a) Normal convolution. (b) Convolution with an expansion factor of 2.

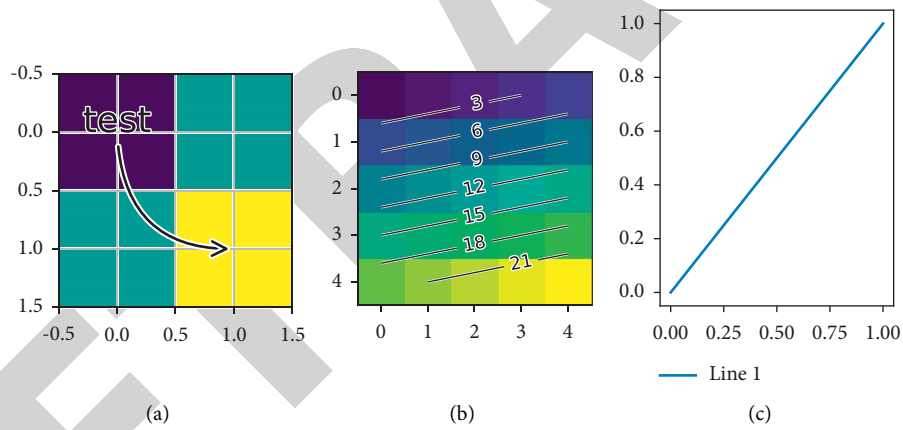


FIGURE 3: Convolutional combination of voids with expansion factor [2 2 2]. (a) Layer 2 convolution output feature map. (b) Layer 1 convolution output feature map. (c) Input feature map.

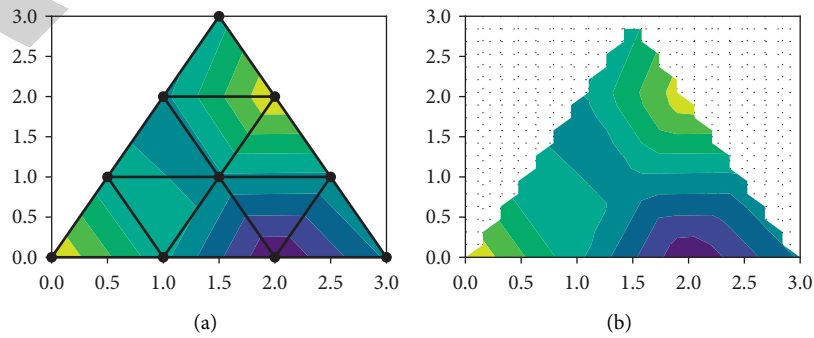


FIGURE 4: Continued.

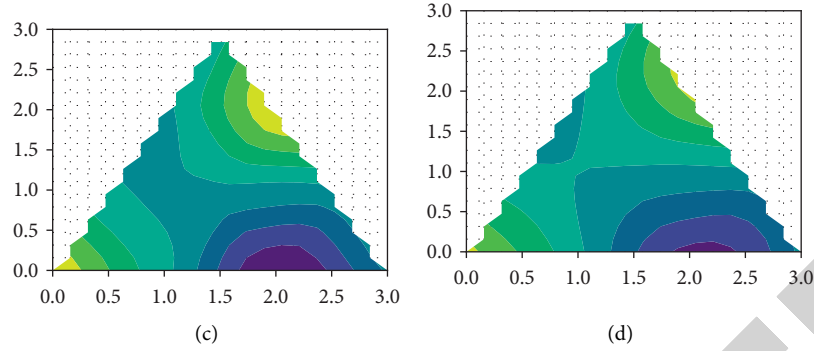


FIGURE 4: Convolutional combination of voids with expansion factor [1 2 9]. (a) Layer 2 convolution output feature map. (b) Layer 1 convolution output feature map. (c) Input feature map.

TABLE 1: Parameters of convolutional module 4 in the new network.

Layer	Operator	Rate	Stride	Padding	Output size
Input	—	—	—	—	$69 \times 69 \times 512$
Conv4_1	[3, 3, 256, 512] conv ReLU	1 —	1 —	1 —	$69 \times 69 \times 512$
Conv4_2	[3, 3, 512, 512] conv ReLU	3 —	1 —	1 —	$65 \times 65 \times 512$
Conv4_3	[3, 3, 512, 512] conv ReLU	5 —	1 —	1 —	$57 \times 57 \times 512$
Pool4	[2] max pool	—	2	0	$28 \times 28 \times 512$

5. Crack Identification Experiments

5.1. Experimental Results and Analysis. The new network was tested using the same test set and the results were compared with those of FCN-8s, as given in Table 2.

As given in Table 2, the new network has a reduced correct rate compared to the FCN-8s background, while the correct rate for cracks has increased by 8.64%, which shows that the improvement to convolution module 4 is effective. By expanding the field of perception of the convolution in convolution module 4, the network is able to extract more complete information about these cracks and better distinguish between cracks and their similarities. Figure 5 shows a picture of cracks detected by FCN-8s and the new network, and Figure 5 shows a zoomed-in view of boxed section in Figure 6.

The reduction in correctness of the new network compared to the FCN-8s background, as given in Table 2, is due to the convolution of a larger field of perception, which can cause some loss of detailed information. When the image background is more complex, the impact caused by this part of information will likely become apparent. As shown in Figure 7, the folded parts present in their images are detected as cracks on a large scale.

It was also found that the new network performed better than FCN-8s for interference on rough concrete surfaces, as shown in Figure 8. FCN-8s detected more uneven parts of rough concrete surfaces as cracks. This is due to the fact that the unevenness of the concrete surface is more uniform, and some of the image detail information lost due to the larger receptive field do not affect the network's learning, while the

TABLE 2: Results of various types of detection for FCN-8s and the new network model.

Type	FCN-8s	New network
Pixel accuracy	0.9815	0.9716
Mean accuracy	0.8247	0.8654
Crack accuracy	0.6721	0.7587
Background accuracy	0.9258	0.9174

larger convolutional receptive field allows the network to better learn the difference between rough concrete surfaces and cracks.

In summary, the new network built by expanding the convolution field in convolution module 4 by means of cavity convolution can effectively improve the detection accuracy of cracks and has a good effect on rough concrete surfaces, but is not suitable for the detection of complex parts such as folds and smears in the background. Cracks are a concern to us and we want to improve the detection of cracks as much as possible, so the new network meets our needs to a certain extent.

5.2. Test Results. The test results of FCN-8s and the new network are given in Table 3. As the new dataset is from a different region than the training set of the network, the correct crack rate in the test results of both FCN-8s and the new network has decreased compared to the previous one. As this test set was not adjusted for difficulty and concrete surfaces in most of the images were more uniform and flat, the new network's detection of the background improved

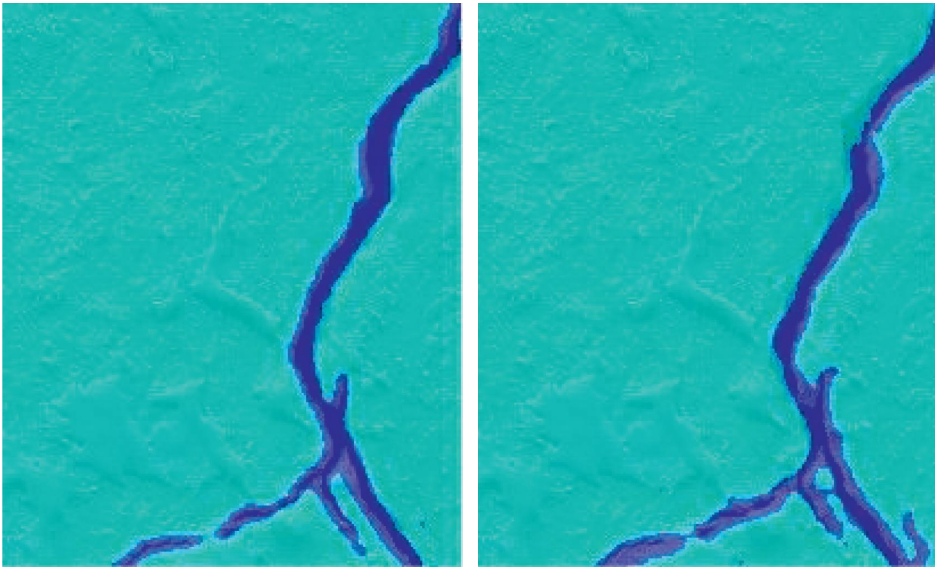


FIGURE 5: Partial enlargement of FCN-8s and new network fracture detection results.

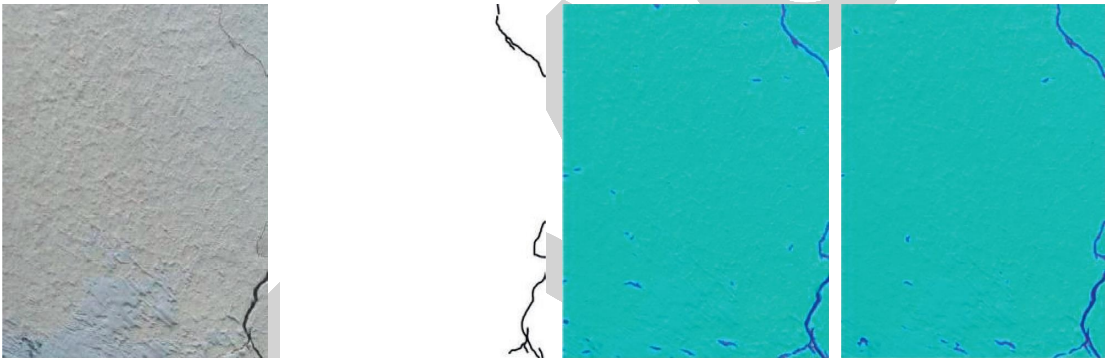


FIGURE 6: Crack detection results of FCN-8s and the new network.



FIGURE 7: FCN-8s and new network concrete crease detection results.

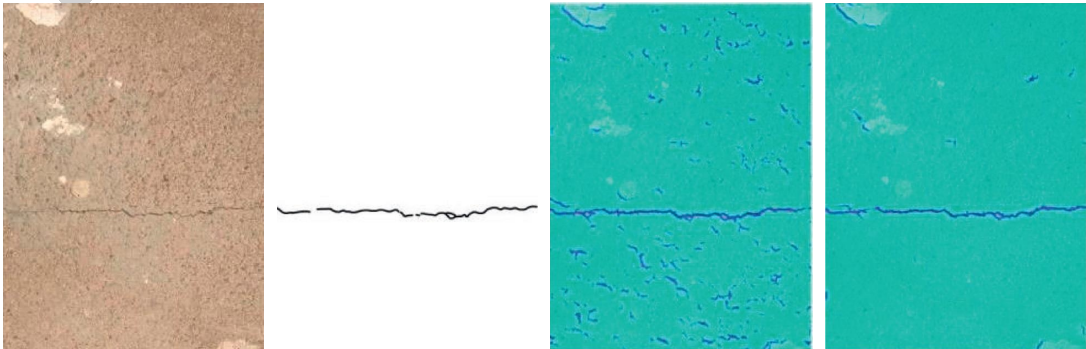


FIGURE 8: FCN-8s and new network coagulation rough surface inspection results.

TABLE 3: Results of various types of detection for FCN-8s and the new network model.

Type	FCN-8s	New network
Pixel accuracy	0.9875	0.9816
Mean accuracy	0.7247	0.8154
Crack accuracy	0.5721	0.6587
Background accuracy	0.98258	0.9874

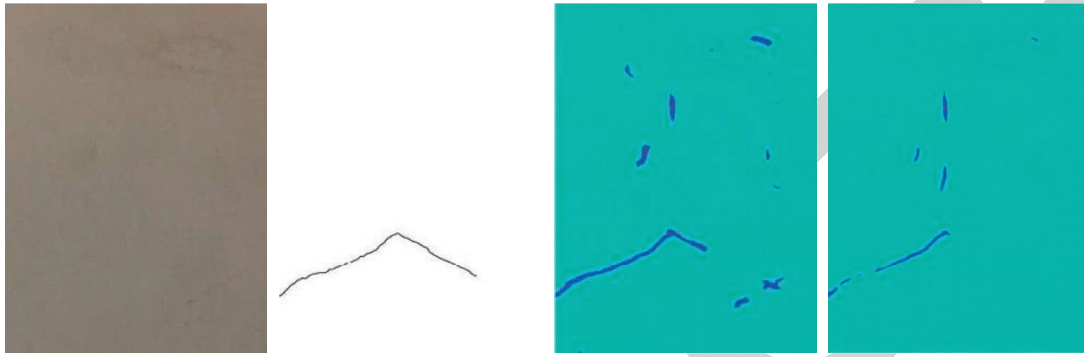


FIGURE 9: FCN-8s and new network detection results.

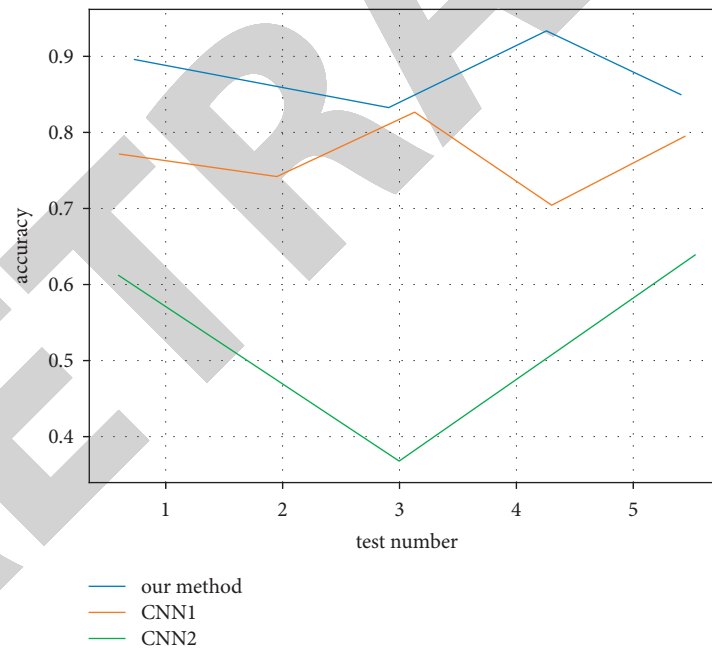


FIGURE 10: Classification accuracy of different models.

significantly from the previous results, and the difference between the new network and FCN-8s in the correct background rate was reduced from 1.02% to 0.33%. On the new dataset, the new network improved the crack correctness metric by 13.09% compared to FCN-8s, and the difference between the two was greater than the test results on the original dataset. This means that the new network performs better on normal cracked images (those with a

more homogeneous concrete surface). The test images in the new dataset are shown in Figure 9, where the new network is more effective in detecting cracks in normal concrete with a flat surface.

The results of the three types of convolutional neural networks are shown in Figure 10. The relationship between the mean square error and the number of iterations for the first group of experiments is shown in Figure 11.

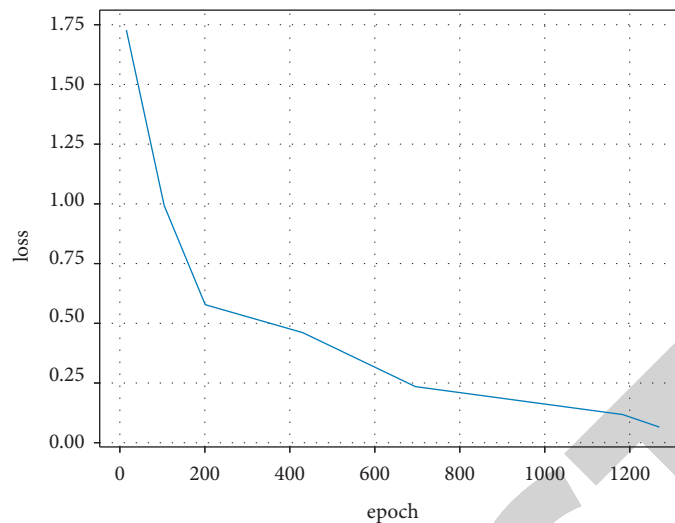


FIGURE 11: Variation of mean squared error.

6. Conclusion

Traditional concrete image-based crack detection uses image processing, which requires high image preprocessing techniques, and the results are susceptible to factors, such as illumination and noise. In this paper, full convolutional neural networks FCN-8s, FCN-16s, and FCN-32s are applied to the detection of apparent cracks in concrete. The correct crack detection rate of the FCN-8s model was 0.6721 when tested, while the new network model had a correct crack detection rate of 0.7585, a significant improvement in the correct crack detection rate.

Data Availability

The data used to support the findings of this study are available from the corresponding author upon request.

Conflicts of Interest

The authors declare that they have no conflicts of interest.

Acknowledgments

This study was sponsored in part by the Fundamental Research Funds for the Central Universities (DL12CB03).

References

- [1] P. Guo, W. Meng, and Y. Bao, "Automatic identification and quantification of dense microcracks in high-performance fiber-reinforced cementitious composites through deep learning-based computer vision," *Cement and Concrete Research*, vol. 148, Article ID 106532, 2021.
- [2] R. Kravchuk and E. N. Landis, "Acoustic emission-based classification of energy dissipation mechanisms during fracture of fiber-reinforced ultra-high-performance concrete," *Construction and Building Materials*, vol. 176, pp. 531–538, 2018.
- [3] A. I. B. Farouk and Z. Jinsong, "Prediction of Interface Bond strength between ultra-high-performance concrete (UHPC) and normal strength concrete (NSC) using a machine learning approach," *Arabian Journal for Science and Engineering*, vol. 47, no. 4, pp. 5337–5363, 2022.
- [4] P. R. Prem, M. Verma, A. R. Murthy, and P. S. Ambily, "Smart monitoring of strengthened beams made of ultrahigh performance concrete using integrated and nonintegrated acoustic emission approach," *Structural Control and Health Monitoring*, vol. 28, no. 5, 2021.
- [5] S. Mahjoubi, W. Meng, and Y. Bao, "Auto-tune learning framework for prediction of flowability, mechanical properties, and porosity of ultra-high-performance concrete (UHPC)," *Applied Soft Computing*, vol. 115, Article ID 108182, 2022.
- [6] J. Wang, C. Liu, and Y. J. Kim, "Artificial Intelligence for Real-Time Crack Detection of Ultra-high-performance Concrete," *Special Publication*, vol. 350, pp. 153–166, 2021.
- [7] R. Solhmirzaei, H. Salehi, V. Kodur, and M. Z. Naser, "Machine learning framework for predicting failure mode and shear capacity of ultra high performance concrete beams," *Engineering Structures*, vol. 224, Article ID 111221, 2020.
- [8] Y. Jiao, Y. Zhang, M. Guo, L. Zhang, H. Ning, and S. Liu, "Mechanical and fracture properties of ultra-high performance concrete (UHPC) containing waste glass sand as partial replacement material," *Journal of Cleaner Production*, vol. 277, Article ID 123501, 2020.
- [9] J. Y. Wang, Z. Z. Chen, and K. Wu, "Properties of calcium sulfoaluminate cement made ultra-high performance concrete: tensile performance, acoustic emission monitoring of damage evolution and microstructure," *Construction and Building Materials*, vol. 208, pp. 767–779, 2019.
- [10] J. A. García, J. F. Gómez, and N. T. Castellanos, "Properties prediction of environmentally friendly ultra-high-performance concrete using artificial neural networks," *European Journal of Environmental and Civil Engineering*, vol. 26, no. 6, pp. 2319–2343, 2020.
- [11] I. H. Yang, C. Joh, and B. S. Kim, "Flexural strength of large-scale ultra high performance concrete prestressed T-beams," *Canadian Journal of Civil Engineering*, vol. 38, no. 11, pp. 1185–1195, 2011.
- [12] J. A. García, "Artificial neural network model for strength prediction of ultra-high-performance concrete," *ACI Materials Journal*, vol. 118, no. 4, pp. 3–14, 2021.

- [13] H. V. Le, T. U. Kim, S. Khan et al., "Development of low-cost Wireless sensing System for Smart ultra-high performance concrete," *Sensors*, vol. 21, no. 19, p. 6386, 2021.
- [14] S. Ahmad, I. Hakeem, and M. Maslehuddin, "Development of an optimum mixture of ultra-high performance concrete," *European Journal of Environmental and Civil Engineering*, vol. 20, no. 9, pp. 1106–1126, 2016.
- [15] P. An, Z. Wang, and C. Zhang, "Ensemble unsupervised autoencoders and Gaussian mixture model for cyberattack detection," *Information Processing & Management*, vol. 59, no. 2, Article ID 102844, 2022.
- [16] D. Y. Yoo, H. O. Shin, and Y. S. Yoon, "Ultrasonic monitoring of setting and strength development of ultra-high-performance concrete," *Materials*, vol. 9, no. 4, 294 pages, 2016.
- [17] A. Marani, A. Jamali, and M. L. Nehdi, "Predicting ultra-high-performance concrete Compressive strength using Tabular Generative Adversarial networks," *Materials*, vol. 13, no. 21, Article ID 4757, 2020.
- [18] S. Abbas and M. L. Nehdi, "Mechanical Behavior of ultrahigh-performance concrete Tunnel lining Segments," *Materials*, vol. 14, no. 9, Article ID 2378, 2021.
- [19] X. Wang, D. Liu, Y. Zhang, and Y. Jiao, "Fracture Characterization of ultra-high performance concrete Notched beams under the Influence of different material factors based on acoustic emission technique," *Materials*, vol. 14, no. 16, Article ID 4608, 2021.
- [20] S. Harenberg, M. Pahn, V. Malárics-Pfaff et al., "Digital image correlation strain measurement of ultra-high-performance concrete-prisms under static and cyclic bending-tensile stress," *Structural Concrete*, vol. 20, no. 4, pp. 1220–1230, 2019.
- [21] F. Ma, M. Deng, and Y. Yang, "Experimental study on internal precast beam-column ultra-high-performance concrete connection and shear capacity of its joint," *Journal of Building Engineering*, vol. 44, Article ID 103204, 2021.
- [22] L. S. Lv, J. Y. Wang, R. C. Xiao, M. S. Fang, and Y. Tan, "Influence of steel fiber corrosion on tensile properties and cracking mechanism of ultra-high performance concrete in an electrochemical corrosion environment," *Construction and Building Materials*, vol. 278, Article ID 122338, 2021.